

Kibble–Zurek scaling of the one-dimensional Bose–Hubbard model at finite temperatures

Werner Weiss,^{1,*} Matthias Gerster,¹ Daniel Jaschke,² Pietro Silvi,³ and Simone Montangero^{1,4,5}

¹*Institute for Complex Quantum Systems & Center for Integrated Quantum Science and Technology, Ulm University, Albert-Einstein-Allee 11, 89069 Ulm, Germany*

²*Department of Physics, Colorado School of Mines, Golden, CO 80401, United States of America*

³*Institute for Theoretical Physics, Innsbruck University, A-6020 Innsbruck, Austria*

⁴*Theoretische Physik, Universität des Saarlandes, D-66123 Saarbrücken, Germany*

⁵*Dipartimento di Fisica e Astronomia “G. Galilei”, Università degli Studi di Padova, I-35131 Padova, Italy*

(Dated: November 14, 2018)

We use tensor network methods — Matrix Product States, Tree Tensor Networks, and Locally Purified Tensor Networks — to simulate the one-dimensional Bose–Hubbard model for zero and finite temperatures in experimentally accessible regimes. We first explore the effect of thermal fluctuations on the system ground state by characterizing its Mott and superfluid features. Then, we study the behavior of the out-of-equilibrium dynamics induced by quenches of the hopping parameter. We confirm a Kibble–Zurek scaling for zero temperature and characterize the finite temperature behavior, which we explain by means of a simple argument.

PACS numbers: 05.30.Jp,37.10.Jk,03.75.Lm,03.75.Gg,64.70.Tg,05.10.-a

I. INTRODUCTION

Ultracold quantum gases in optical lattices offer the possibility to explore the behavior of condensed matter systems on a controllable testbed [1–7]. This platform using interference of laser beams to create spatial standing waves is well-suited for tailoring a variety of lattice structures in three [8] or less dimensions [9–11]. Systems of bosons in an optical lattice can be described by the Bose–Hubbard model. First introduced in the 1960s by Gersch and Knollmann [12], it became very helpful in understanding the superfluid to Mott insulator phase transition [13, 14] and has been realized in a multitude of experiments (for an overview see, e.g. Ref. [15]). In particular, the one-dimensional setting has been studied in great depth over the years and is characterized by rich physics, one of the reasons being the occurrence of a multicritical point with a Berezinskii–Kosterlitz–Thouless (BKT) transition [13, 14].

For a long time the theoretical and numerical work on this model has concentrated on the zero-temperature limit, which is a valid approximation for many experimental setups. Nevertheless, characterizing the impact of thermal fluctuations is an important prerequisite in order to enable a comprehensive understanding of the observed phenomena [16]. An early investigation on the influence of finite temperatures on the Bose–Hubbard model, focusing mostly on the insulating regime, has been carried out in Ref. [17]. This work was followed by further theoretical [18–22] and experimental studies [23–27].

In addition to the equilibrium physics of the model, the investigation of dynamical processes, arising from tuning

the system’s parameters, are of great interest [28–33], especially towards engineering complex phases in quantum gases. An important scenario in this context are quasi-adiabatic quenches across quantum phase transitions, for which the Kibble–Zurek hypothesis [34–37] offers a simple and intuitive theoretical framework, yet allowing for a quantitative understanding of the formation of defects when crossing a quantum critical point. The Kibble–Zurek mechanism has been tested in a plethora of theoretical and experimental settings, including the Bose–Hubbard model itself [38–40]. Also in this context, attempts have been made to address thermal effects [41–43].

In this work we focus on the one-dimensional Bose–Hubbard model on chains of moderate sizes in the range of current experiments. We analyze the effects of finite temperature on two types of scenarios of experimental interest: First, we characterize the properties of the system after being prepared in an initial thermal state under a given set of constant system parameters. We study to which extent the properties of the insulating and superfluid phase persist at finite temperatures, expanding on previous results [17]. Secondly, we explore the dynamics of the system triggered by a linear quench in the particle hopping parameter. We verify the predicted Kibble–Zurek scaling at zero temperature [38], and then study deviations from this behavior with rising initial temperature. We propose a simple argument, capable of providing a quantitatively correct prediction of the obtained finite-temperature results.

Our analysis is based on numerical simulations using Tensor Network (TN) methods, which are well established as a powerful tool for simulating low-dimensional strongly-correlated many-body systems [44–46]. At the core of the analysis, we employ Locally Purified Tensor Networks (LPTN) [47–49], a tailored variational ansatz

* werner.weiss@uni-ulm.de

capable of representing thermal equilibrium states, as well as to perform real-time evolution for time-dependent Hamiltonians and Lindblad master equations. Previously, this method has been successfully applied to Quantum Ising chains [50]. In the zero-temperature limit, we complement our results using Matrix Product State (MPS) [51] and Tree Tensor Network (TTN) [52, 53] simulations.

The remainder of this paper is structured as follows: In Sec. II we introduce the model and the notation, and study the properties of the system at equilibrium by characterizing the insulating (Sec. II A) and superfluid (Sec. II B) features of its thermal states. The collected results are summarized in a finite-temperature state diagram (Sec. II C). In Sec. III we extend our analysis to dynamical processes by quenching the system in the hopping parameter, first at zero temperature (Sec. III A), and then at finite temperatures (Sec. III B). In Sec. IV we draw our conclusions.

II. EQUILIBRIUM PROPERTIES

We consider a 1D Bose–Hubbard lattice [13] described by the Hamiltonian

$$H = -J \sum_{j=1}^{L-1} (b_j^\dagger b_{j+1} + \text{h.c.}) + \frac{U}{2} \sum_{j=1}^L n_j(n_j - 1) - \mu \sum_{j=1}^L n_j. \quad (1)$$

Here, b_j (b_j^\dagger) is a bosonic annihilation (creation) operator obeying $[b_j, b_{j'}^\dagger] = \delta_{jj'}$, and $n_j = b_j^\dagger b_j$ is the particle number operator on site j . L is the length of the chain, which we assume to have open boundaries. The coupling J determines the hopping strength, while U and μ represent the on-site repulsion strength and the chemical potential, respectively. By setting $U = \hbar = k_B = 1$, k_B being Boltzmann’s constant, we fix the units of energy E , time t , and temperature T .

Depending on the values of the parameters J and μ , the ground state of H at zero temperature exhibits different phase properties [13, 14, 54]. Two phases emerge: In the *Mott insulator* phase, which in the (J, μ) -plane of the phase diagram appears as “lobes” [13] in proximity of the $J = 0$ axis, the bosonic particles are localized at single lattice sites and the filling factor $\varrho = N/L$ (where $N = \langle \sum_{j=1}^L n_j \rangle$ is the total number of particles in the system) is pinned to integer values, depending on the chemical potential μ . Moreover, this phase has a finite energy gap ΔE and it is incompressible, i.e. $\partial\varrho/\partial\mu = 0$. In contrast, a *superfluid* phase appears for large enough J , in which the bosons are delocalized over the entire lattice. In this phase, ϱ is in general not integer, hence it is compressible $\partial\varrho/\partial\mu > 0$. The superfluid phase is gapless, i.e. $\Delta E = 0$,

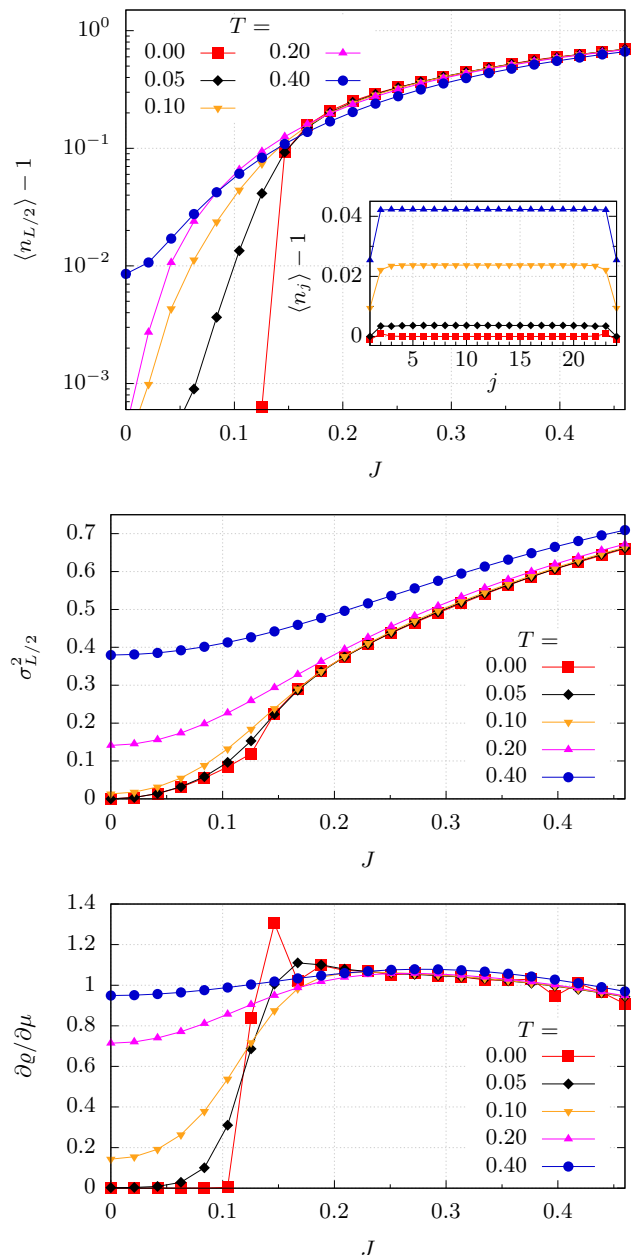


FIG. 1. (Color online) On-site occupation $\langle n_{L/2} \rangle$ (top panel), variance $\sigma_{L/2}^2$ (middle panel), and compressibility $\partial\varrho/\partial\mu$ (bottom panel), determined via a linear fit of $\varrho(\mu)$ in the interval $\mu \in [0.425, 0.575]$ as a function of J for various temperatures T , measured at the center of a chain with $L = 24$ sites for $U = 1$ and $\mu = 1/2$. The inset in the top panel shows the particle occupations along the whole chain, for fixed $J = 0.08$.

and its quasi-long-range order is expected to disappear at any finite temperature in the thermodynamic limit.

In the remainder of this section, we characterize the equilibrium properties of the Bose–Hubbard chain at finite temperatures $T > 0$. In particular, we aim to quantify to which extent the thermal equilibrium states keep their Mott- or superfluid-phase features when increasing the temperature at a finite size L . We perform

this characterization numerically, using an LPTN ansatz state, representing the thermal many-body density matrix $\rho = e^{-\beta H} / \text{Tr}[e^{-\beta H}]$, with $\beta = 1/T$. For zero temperature, an MPS can be used instead of an LPTN. In this sense, the LPTN extends the MPS picture, valid at $T = 0$, to finite temperatures (see also Appendix A). Clearly, the numerical treatment implies a truncation of the bosonic local Fock spaces to a finite cutoff dimension d , in order to carry out the numerical simulation. The effect of this truncation is tunable, and negligible as long as high local occupation numbers are energetically suppressed, i.e. as long as the parameters J , μ , and T do not become too large (compared to $U = 1$). Here, we adopt up to $d = 5$, which we verified to be sufficient for the parameter regime studied here, see also Appendix B. The lengths of the simulated systems range from $L = 16$ to $L = 32$ sites. We target via LPTN the grand canonical ensemble density matrix, and, in what follows, we use $\mu = 1/2$. Along this line in the phase diagram, the transition from the Mott insulator to the superfluid is known to be a second order quantum phase transition in the $T = 0$ case [13], taking place at a critical hopping strength of $J_c \approx 0.13$ [14]. Let us stress that this scenario is not to be confused with the phase transition at fixed particle filling $\varrho \in \mathbb{N}$, which is of the BKT type [13] and will play a role in the real-time dynamics.

A. Characterization of Mott insulating features

We start by quantifying the Mott-like character of the system, as a function of both J and T . In order to do so, we use the on-site particle occupations $\langle n_j \rangle$ and their variance

$$\sigma_j^2 = \langle n_j^2 \rangle - \langle n_j \rangle^2, \quad (2)$$

as well as the compressibility $\partial\varrho/\partial\mu$. A necessary condition for Mott insulating states are localized particles, leading to integer on-site occupation numbers $\langle n_j \rangle \in \mathbb{N}$. This behavior is accompanied by small variances $\sigma_j^2 \approx 0$ and a vanishing compressibility. Specifically, the particle occupation is one (i.e. $\langle n_j \rangle = 1$) in the first Mott lobe which is crossed by the $\mu = 1/2$ line studied here. In contrast, outside of the Mott insulating phase, the occupation can attain any value $\langle n_j \rangle \in \mathbb{R}^+$ and the compressibility is strictly larger than zero. This finite compressibility can either be induced by thermal fluctuations, when T becomes large enough to overcome the on-site repulsion, or by quantum fluctuations, even at zero temperature, when J becomes large enough to favor delocalized particles.

In Fig. 1, we show the numerically obtained occupation numbers, variances, and compressibilities as a function of the coupling J for various temperatures $T \in [0, 0.4]$. Here the system size is $L = 24$ sites. In order to avoid boundary effects, we measure local quantities close to the center of the chain. As shown in Fig. 1, the on-site particle occupation at $T = 0$ is indeed exactly $\langle n_j \rangle = 1$ in

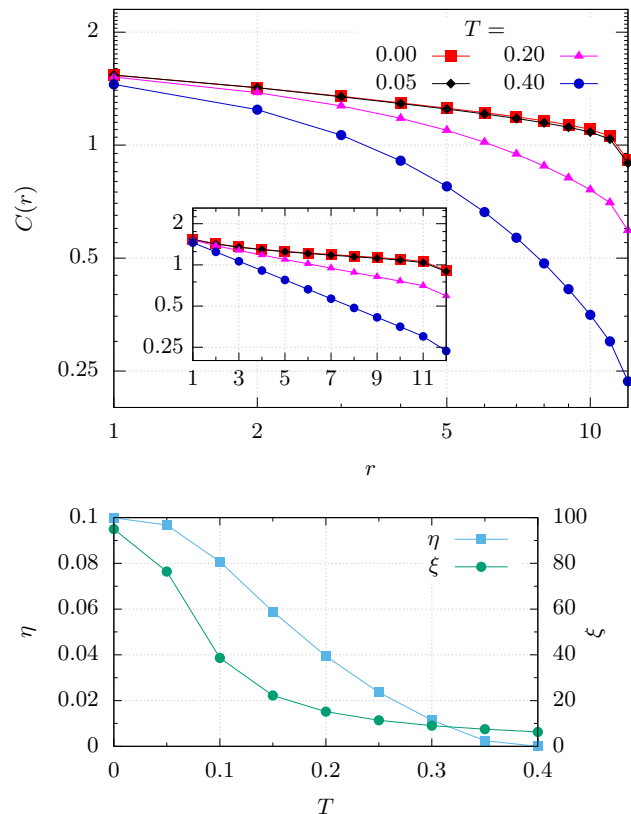


FIG. 2. (Color online) Upper panel: Correlation functions $C(r)$ as a function of the distance r in double-logarithmic scale (main plot), and semi-logarithmic scale (inset plot) for fixed $J = 0.46$, $U = 1$, $\mu = 1/2$ and various temperatures T . The system size is $L = 24$. Lower panel: Fit parameters η and ξ , obtained by fitting Eq. (3) to the correlation functions $C(r)$.

the interval $0 \leq J \leq J_c$, while for $J > J_c$ a monotonous increase can be observed. This abrupt behavior is replaced by a smoother transition with rising temperature, actually reducing the range of J supporting a Mott-like emergent behavior with $\langle n_j \rangle = 1$. The compressibility $\partial\varrho/\partial\mu$ exhibits a similar behavior; we remark, however, that this quantity is more prone to finite-size effects due to the involved numerical derivative (see Appendix B). For small temperatures $T < T^* \approx 0.2$, we observe that the variance is approximately insensitive to T , indicating a survival of Mott-like features at least up to these temperatures. For this reason, the temperature T^* has also been referred to as the “melting temperature” of the Mott insulator [17].

B. Characterization of superfluid features

In order to identify superfluid features, we study the behavior of the two-point hopping correlation function $C(r) = \langle b_j^\dagger b_{j+r} \rangle$. While in higher dimensions this correlation function exhibits long-range order in the super-

fluid phase, in one dimension the Mermin-Wagner theorem [55, 56] prohibits a spontaneous breaking of the U(1) symmetry. Therefore, the superfluid phase merely exhibits quasi-long-range order in 1D, characterized by algebraically decaying correlation functions $C(r) \propto r^{-\eta}$. In contrast, outside of the superfluid phase order occurs only at a finite correlation length ξ , which is signaled by an exponential decay $C(r) \propto e^{-r/\xi}$. The quasi-long-range order can either be destroyed by thermal fluctuations, i.e. when T dominates over J , or, even at zero temperature, when J becomes small and the particles crystallize due to density-density interactions, see the Mott insulator phase.

In order to illustrate this behavior, we plot the correlation functions $C(r) = \langle b_{L/2}^\dagger b_{L/2+r} \rangle$ for a fixed value $J > J_c$ and different temperatures in Fig. 2. Although the finite size of the system (here $L = 24$) makes it difficult to precisely extract the exponent η or the correlation length ξ , one can nevertheless detect the crossover from a power-law to an exponential decay when raising the temperature, hinting at a gradual loss of coherence. In order to quantify this observation, we fit the correlation functions with

$$C(r) \propto r^{-\eta} \exp\left(-\frac{r}{\xi}\right), \quad (3)$$

and plot the fit parameters η and ξ as a function of T (see lower panel of Fig. 2): For small temperatures, we obtain $\xi \gg L$, meaning a predominantly algebraic decay, while for larger temperatures we have $\xi < L$ and η small, signaling a mainly exponential decay.

As a secondary approach to quantify the superfluid-like nature of a given state ρ , we define and numerically calculate the “finite-size correlation length” ξ_L as follows:

$$\xi_L = \sqrt{\frac{\sum_{j,k=1}^L (j-k)^2 \langle b_j^\dagger b_k \rangle}{\sum_{j,k=1}^L \langle b_j^\dagger b_k \rangle}}. \quad (4)$$

The two definitions of ξ coincide (neglecting a constant prefactor) when ξ is larger than the lattice spacing, but smaller than the system size: $\xi_{L \gg \xi} = \xi$. If, however, the true correlation length becomes comparable to or larger than the system size, ξ_L is upper-bound by a constant proportional to L . This bound can be shown by considering the limiting case of a constant correlation function $C(r) \rightarrow \varrho$, which is the asymptotically exact ground state correlation function of H in the limit $J \rightarrow \infty$, since $\eta(J \rightarrow \infty) \rightarrow 0$. Obviously, the true correlation length is diverging in this case ($\xi \rightarrow \infty$), but for ξ_L we get

$$\xi_L = \sqrt{\frac{\sum_{j,k=1}^L (j-k)^2 \varrho}{\sum_{j,k=1}^L \varrho}} = \sqrt{\frac{L^2 - 1}{6}} \xrightarrow{L \rightarrow \infty} \frac{L}{\sqrt{6}}. \quad (5)$$

More in general, one can show that for $L \rightarrow \infty$ the proportionality $\xi_L \propto L$ is valid for any algebraically decaying correlation function, if its exponent η is in the range

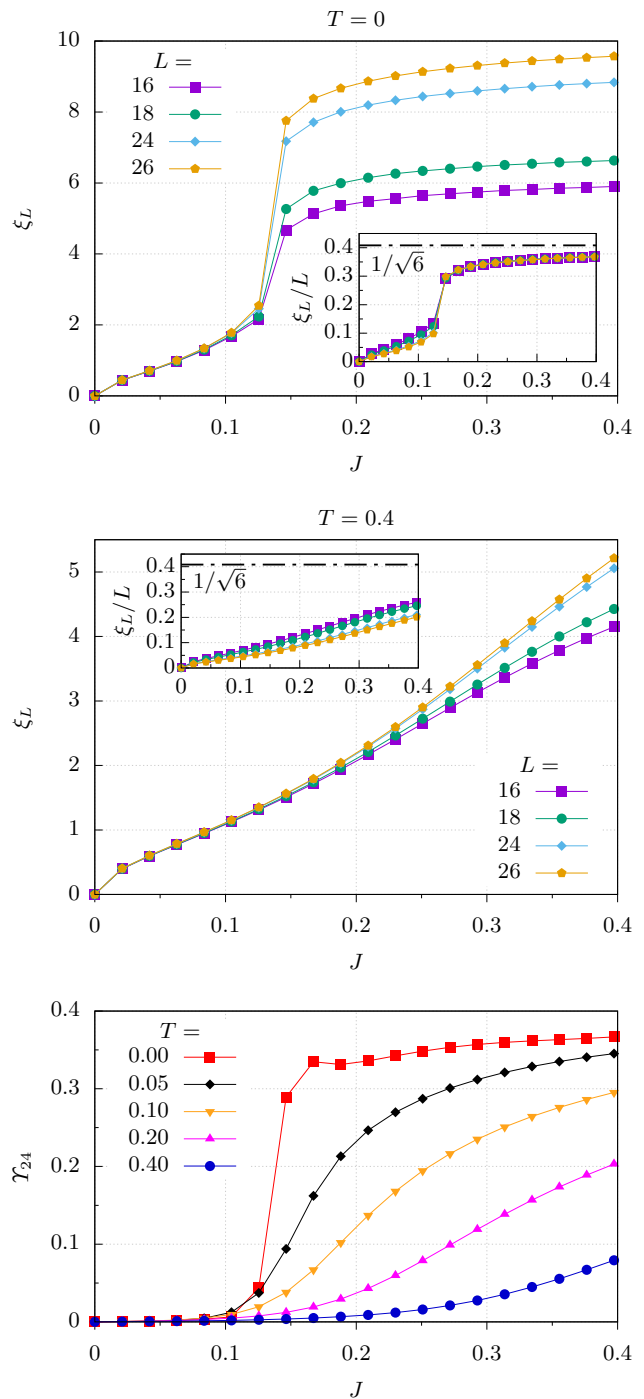


FIG. 3. (Color online) Finite-size correlation length ξ_L as a function of J for several system sizes L and two different temperatures $T = 0$ (top panel) and $T = 0.4$ (middle panel), with fixed $U = 1$, $\mu = 1/2$. The insets show ξ_L/L for the same data, together with the upper bound $1/\sqrt{6}$. Bottom panel: Quantifier for superfluidity γ_{24} , calculated with $\Delta L = 2$ according to Eq. (6), for various temperatures $T \in [0, 0.4]$.

$0 \leq \eta < 1$. This condition holds throughout the superfluid phase [14, 57]. Consequently, a diverging correlation length ξ can be detected by monitoring whether the ratio ξ_L/L approaches a constant larger than zero when increasing L . If, on the other hand, this ratio tends to zero for increasing L , the correlation length is finite.

We illustrate this idea in Fig. 3 (upper two panels), both for zero and non-zero temperature. Clearly, the more superfluid-like the system, the more ξ_L diverges with the system size L . Based on this observation, we quantify the superfluid-like nature of a thermal state ρ via

$$\Upsilon_L(J, T) = \frac{\xi_{L+\Delta L}(J, T) - \xi_L(J, T)}{\Delta L}, \quad (6)$$

measuring incremental growth of ξ_L while increasing the system size by ΔL . In the bottom panel of Fig. 3 we plot Υ_{24} with $\Delta L = 2$ as a function of J for different temperatures T . At zero temperature, a sharp, discontinuous increase of Υ_L at $J \approx J_c$ separates the Mott insulating phase with vanishing Υ_L from the superfluid phase with non-zero Υ_L . Higher temperatures gradually smooth out the transition and push the regime of superfluid-like correlations to larger and larger values of J .

C. State diagram for finite system sizes at finite temperatures

Having developed quantifiers for both the Mott-like and the superfluid-like character of the system, we can summarize the data from the previous two subsections in a single graph, leading to the finite-size state diagram shown in Fig. 4. The intensity of the blue color corresponds to the deviation $\Theta(J, T)$ of the variance $\sigma_{L/2}^2(J, T)$ from its maximal value in the considered intervals of J and T . More specifically,

$$\Theta(J, T) = \max_{J, T} \left[\sigma_{L/2}^2(J, T) \right] - \sigma_{L/2}^2(J, T) \quad (7)$$

with the variance $\sigma_{L/2}^2(J, T)$ as defined in Eq. (2). Consequently, the intensity of the blue color encodes the presence of Mott-like features. Similarly, the intensity of the orange color encodes the occurrence of superfluid-like features measured via $\Upsilon_L(J, T)$, as defined in Eq. (6).

For $T = 0$ the sharp transition between Mott insulator phase and superfluid phase at $J \approx J_c$ is clearly visible in Fig. 4. For small enough temperatures and sufficiently far away from J_c the essential features of the two phases survive. A larger and larger “thermal region”, where thermal fluctuations prevent any type of order, opens up around J_c when raising the temperature.

III. DYNAMICS

We now discuss some aspects of time evolution, i.e. the out-of-equilibrium dynamics in the Bose–Hubbard

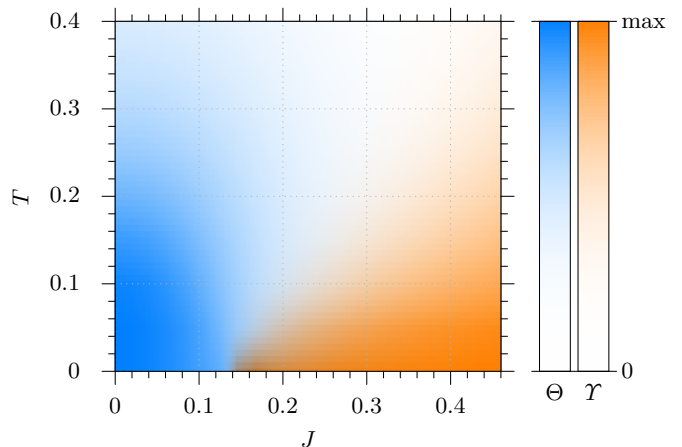


FIG. 4. (Color online) Characterization of Mott-like features (blue) and superfluid-like features (orange) as a function of hopping strength J and temperature T (for fixed $U = 1$, $\mu = 1/2$), based on the analysis described in Secs. II A and II B. White color corresponds to the “thermal region”. The system size is $L = 24$.

model. In particular, we are interested in analyzing the behavior of the system when exposed to linear-ramp quenches in the hopping strength J across the phase transition. This is the typical scenario investigated in the framework of the Kibble–Zurek mechanism (KZM) [34, 35]. As before, we start from the zero temperature behavior and then proceed to analyze the impact of finite temperatures. We use the following quench protocol:

- (i) The starting point is the equilibrium state ρ_0 of the Hamiltonian H for $J = 0$, $\mu = 1/2$. Since the coupling term vanishes in this case, ρ_0 is always a product state. At zero temperature, ρ_0 is the pure state composed of the perfect Mott insulator state $|\Psi\rangle$ with filling one, i.e. $|\Psi\rangle = |1\rangle_1 \dots |1\rangle_L$, while at finite temperature $\rho_0 = e^{-\beta H_0} / \text{Tr}[e^{-\beta H_0}]$.
- (ii) The initial state ρ_0 is evolved via unitary time evolution $\dot{\rho} = -i[H(t), \rho]$ in the time interval $t \in [-\tau_Q/2, \tau_Q/2]$, where τ_Q is the duration of the quench. The Hamiltonian is time-dependent through a linear ramp in the hopping strength

$$J(t) = \frac{2J_c}{\tau_Q} t + J_c, \quad (8)$$

which is chosen to be symmetric around the critical point J_c , such that $J(0) = J_c$ and $J(-\tau_Q/2) = 0$. Since $[H(t), \sum_{j=1}^L n_j] = 0$, the total particle number N is a constant of motion. For $T = 0$ this implies that the dynamics takes place along the line of constant filling $\varrho = 1$ in the phase diagram, which passes through the multicritical point at the tip of the first Mott lobe [13]. The phase transition in this case [58] is of the BKT type [59, 60], and it is located at $J_c \approx 0.30$ [15, 61]. The time evolution of the

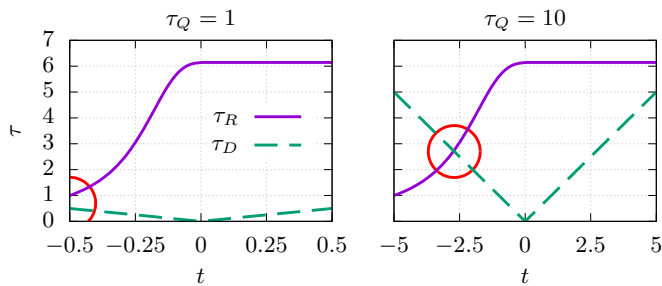


FIG. 5. (Color online) Driving timescale τ_D and relaxation timescale τ_R as a function of time t for a system of $L = 16$ sites undergoing the linear quench of Eq. (8), with fixed $U = 1$, $\varrho = 1$. Left panel: For $\tau_Q < 2$ no intersection of the two timescales exists, hence τ_D is always smaller than τ_R . Right panel: For $\tau_Q \geq 2$ the timescales intersect (depicted by a circle), leading to a nontrivial freeze-out time \hat{t} .

quantum many-body state (computed by means of MPS and LPTN for zero and finite temperature, respectively) is performed numerically with the Time-Evolving Block Decimation (TEBD) [62] algorithm using a Suzuki-Trotter decomposition of the Hamiltonian at second order (see also Appendix A).

- (iii) At the end of the quench, the superfluid correlation length ξ_{fin} is measured using Eq. (4). We then study the behavior of this “defect measure” [36] as a function of the quench duration τ_Q .

A. Quenches at zero temperature

In order to enable an understanding of the essential features of the system’s state after the quench, the KZM provides a simple yet powerful argument relying on a comparison of the system’s internal relaxation timescale $\tau_R(t)$ with the external driving timescale $\tau_D(t)$. This comparison separates the dynamics into two stages: an adiabatic stage when $\tau_R(t) < \tau_D(t)$, and an impulsed (sudden) stage when $\tau_R(t) > \tau_D(t)$. The instant \hat{t} at which the dynamics changes from adiabatic to sudden is called the “freeze-out time”. Based on this simple picture, the KZM predicts that the order properties of the system after the quench are essentially determined by the instantaneous ground state at $\hat{J} = J(\hat{t})$ [35].

For the case of a second order quantum phase transition, the KZM allows for a particularly elegant description of the scaling of the final density of defects as a function of the quench duration. More specifically, if at the critical point the equilibrium correlation length diverges with a critical exponent ν and the energy gap ΔE closes with another critical exponent $z\nu$, the KZM predicts [36] that the final correlation length (after the quench) scales according to

$$\xi_{\text{fin}} \propto \tau_Q^\kappa, \quad \text{where} \quad \kappa = \frac{\nu}{1 + z\nu}, \quad (9)$$

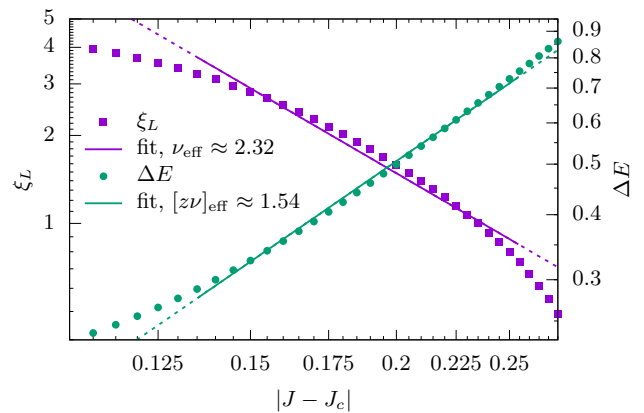


FIG. 6. (Color online) Fitting of the effective critical exponents ν_{eff} and $[z\nu]_{\text{eff}}$ to the equilibrium scaling of ξ_L and ΔE , respectively, as a function of the distance $|J - J_c|$ from the critical point J_c . Note that all axes are logarithmic. The fit interval (marked by non-dashed lines) has been chosen such that it covers the range of freeze-out points \hat{J} for quench times in the interval $3 \leq \tau_Q \leq 15$. The system size is $L = 16$, and $U = 1$, $\varrho = 1$.

i.e. the scaling of the defect density as a function of the quench time is determined by a single constant exponent κ .

Here, however, due to the preservation of the total number of particles induced by the $U(1)$ symmetry, we cross an infinite-order BKT transition which produces quantitative and qualitative deviations from the traditional KZ picture [38, 63]: While the basic idea of identifying the final correlation length with the one at equilibrium at time \hat{t} is in principle still valid, the exponential scaling [64] of the equilibrium quantities $\Delta E(J)$ and $\xi(J)$ near the critical point J_c prevents the derivation of a simple expression like the one in Eq. (9). Nevertheless, following Ref. [38], one can still define “effective” critical exponents ν_{eff} and $[z\nu]_{\text{eff}}$ by approximating the exponentials with power-laws around a sufficiently small interval around the freeze-out point \hat{J} . Obviously, these exponents now depend on \hat{J} and hence also on the quench time τ_Q , but this approach allows one to recover (at least formally) the scaling given in Eq. (9), after replacing κ with an effective exponent $\kappa(\tau_Q)$:

$$\kappa(\tau_Q) = \frac{\nu_{\text{eff}}(\tau_Q)}{1 + [z\nu]_{\text{eff}}(\tau_Q)}. \quad (10)$$

In the following, we will adopt this strategy to verify the validity of the KZM for the quench protocol described above at zero temperature. To this end, we first need to determine the freeze-out times $\hat{t}(\tau_Q)$. We do this numerically, by comparing the relaxation timescale $\tau_R(t) = 1/\Delta E(t)$ with the driving timescale $\tau_D(t) = |(J(t) - J_c)/\dot{J}(t)| = |t|$ [36]. This procedure is illustrated in Fig. 5, for two different quench times τ_Q . In our energy units we have $\Delta E(-\tau_Q/2) = \Delta E(J = 0) = 1$, thus the relaxation timescale is always $\tau_R(-\tau_Q/2) = 1$ at the be-

gining of the quench. Hence, for all $\tau_Q < 2$ the driving timescale $\tau_D(-\tau_Q/2) = \tau_Q/2$ is sufficiently fast that the quench will be completely sudden. On the other hand, if $\tau_Q \geq 2$, there is an intersection of the two timescales and a nontrivial KZM scaling of the final defect density can be expected. In order to verify the KZM in this regime, we numerically determine the effective critical exponents ν_{eff} and $[z\nu]_{\text{eff}}$ as shown in Fig. 6. By fitting power-laws to the equilibrium quantities in the appropriate interval of J , we obtain $\nu_{\text{eff}} = 2.32 \pm 0.2$ and $[z\nu]_{\text{eff}} = 1.54 \pm 0.1$ which is compatible with the numbers reported in Ref. [63]. Inserting these values into Eq. (10) delivers the prediction $\kappa = 0.92 \pm 0.12$ for the scaling of the final correlation length ξ_{fin} after the quench.

In Fig. 7, we show the final correlation lengths ξ_{fin} , measured after simulating the time evolution of the quantum many-body state with the TEBD algorithm, for various values of τ_Q spanning several orders of magnitude. Three regimes can be observed (marked by different shadings):

- Sudden quench regime for $\tau_Q \lesssim 2$: As discussed above, the dynamics may be viewed as driven by a short impulse of duration τ_Q in this regime. The fact that τ_Q is small allows for an approximate integration of the Schrödinger equation via discretization. Such an approximation can be done analytically, resulting in the following expression for the final correlation length (see Appendix C):

$$\xi_{\text{fin}}(\tau_Q) = 2\sqrt{J_c} \tau_Q + \mathcal{O}(\tau_Q^2). \quad (11)$$

For $\tau_Q \ll 1$ this expression is in good agreement with the numerical data, as demonstrated by the orange line in Fig. 7.

- KZM scaling for $2 \lesssim \tau_Q \lesssim 15$: The fact that this regime has an upper bound for τ_Q is due to the finite size of the system (here $L = 16$), implying a saturation value of $L/\sqrt{6}$ for the correlation length (see Eq. (5)). Fitting the exponent κ from the data in the KZM scaling regime yields $\kappa = 0.88 \pm 0.1$, which is in good agreement both with the prediction based on the equilibrium effective critical exponents outlined above and with the experimental and numerical results reported in Ref. [39].
- Saturated regime for $\tau_Q \gtrsim 15$: In this regime, the final correlation length is saturated due to the finite system size. Here, the defect density becomes too small to be resolved in a system of size L and the system appears completely ordered. Larger system sizes shift this regime to larger values of τ_Q (not shown in the figure).

B. Quenches at finite temperatures

In order to gain some (semi-quantitative) understanding of the behavior of the KZ scaling for finite tempera-

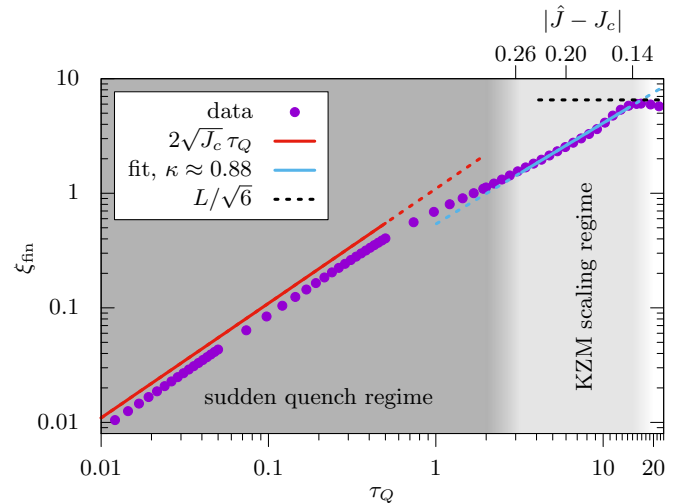


FIG. 7. (Color online) Final correlation length ξ_{fin} as a function of the quench time τ_Q for $T = 0$. Three different regimes can be distinguished: sudden quench regime, KZM scaling regime, and the regime of finite-size saturation. The system size is $L = 16$, and $U = 1$, $\rho = 1$.

tures, it is instructive to first consider the limiting case $T \rightarrow \infty$. Since in this case the thermal state ρ_0 asymptotically approaches the identity, i.e. $\rho_0(T \rightarrow \infty) \rightarrow \mathbb{1}$, the time evolution is trivial and the final state is again the identity: $\rho_{\text{fin}}(T \rightarrow \infty) = \rho_0$. This behavior automatically implies a vanishing KZ exponent κ , because $\xi_{\text{fin}}(\tau_Q) = \xi_0 = 0$. Hence, we expect $\kappa(T \rightarrow \infty) \rightarrow 0$. On the other hand, for $T = 0$ we need to recover the zero-temperature KZ exponent: $\kappa(T \rightarrow 0) \rightarrow \kappa_0$, where κ_0 is determined by the KZM described above. In order to provide a heuristic ansatz for the KZ exponent $\kappa(T)$ at finite temperatures, we resort to an Arrhenius argument. This argument fits because the deviation $\Delta\kappa(T) = \kappa_0 - \kappa(T)$ of the thermal KZ exponent from the zero-temperature KZ exponent can be viewed as a thermally induced quantity: An energy barrier needs to be overcome by means of thermal activation in order to enable an increase of $\Delta\kappa$. Based on this motivation, we use the Arrhenius ansatz [65]

$$\Delta\kappa(T) = \kappa_0 e^{-E_a/T}, \quad (12)$$

where E_a is an activation energy. Since the increase of $\Delta\kappa(T)$ is “activated” by an increasingly dominating population of excited states in the initial thermal density matrix $\rho_0(T)$, the energy gap $\Delta E'$ between the ground and excited state can be considered an appropriate energy scale for the activation energy E_a . As ρ_0 results from the Hamiltonian with $J = 0$ in our protocol, the energy gap is easily seen to be $\Delta E' = \mu$. It is worth mentioning that here the relevant energy gap is the inter-sector gap $\Delta E'$ (i.e. the energy difference between a system with N particles and a system with $N + 1$ particles) because we are working in a grand canonical ensemble. This gap is not the same as the intra-sector gap ΔE employed in the previous section, which is relevant for deter-

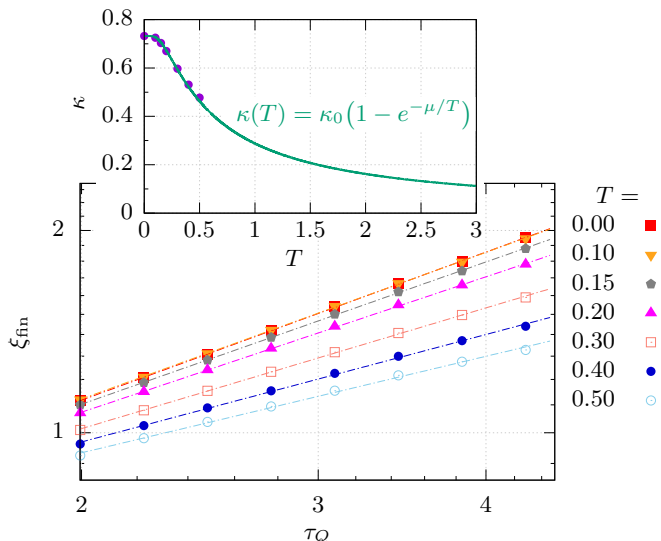


FIG. 8. (Color online) Correlation length ξ_{fin} after the quench as a function of the quench duration τ_Q , for various temperatures T . The dashed lines are linear fits whose slopes determine the KZ exponents $\kappa(T)$. The system size is $L = 16$, and $U = 1$. Upper plot: extracted exponents as a function of T , together with the Arrhenius ansatz indicated in Eq. (13), with $\mu = 1/2$.

mining the freeze-out of the particle-conserving adiabatic time evolution of the ground state at zero temperature.

Combining all assumptions, we predict the following thermal dependence of the KZ exponent:

$$\kappa(T) = \kappa_0 \left(1 - e^{-\mu/T}\right). \quad (13)$$

Figure 8 stresses the validity of this ansatz: In the numerically accessible interval of small temperatures ($T < 0.5$), the determined KZ exponents follow indeed the prediction given in Eq. (13).

IV. CONCLUSION

In this work, we have investigated the properties of the equilibrium and out-of-equilibrium one-dimensional Bose–Hubbard model at finite temperature. In the analysis of equilibrium properties we find, for the considered system sizes, a persistence of both insulating and superfluid features up to a certain temperature depending on the coupling J . Our simulations yield a variety of observable data which characterize the physics of the thermal system. Additionally, theoretical predictions for the system’s quantities at finite temperatures allow for thermometry in an experimental setup [26, 66].

The investigation of the dynamical behavior of the system results in a verification of the Kibble–Zurek scaling for zero temperature, and a good agreement between the proposed Arrhenius-type ansatz and the obtained numerical data for $T > 0$.

Our analysis offers many possible extensions, e.g. investigating certain regions of the J - μ phase diagram where a revival of the Mott insulating phase is expected [14] or, as often found to characterize experimental setups, simulating harmonically confined systems realized by site-dependent chemical potentials [15, 67, 68].

Finally, an essential question is when the scenario of evolving a mixed state with a unitary time evolution following the von Neumann equation applies. Throughout this work we consider the case where the timescale of the quench is much shorter than the timescale of the system to reach the thermal equilibrium. This condition is normally fulfilled if we prepare the initial thermal state and are able to largely decouple the system from the environment. If, instead, the quench timescale is comparable to or larger than the relaxation timescale, one has to include open-system dynamics into the calculations [69, 70]. This case is left for future studies and requires a careful choice of Lindblad operators [71–74] for Markovian dynamics or evolution of non-Markovian systems [75, 76].

ACKNOWLEDGMENTS

We thank F. Tschirsich for discussions and additional numerical checks. Numerical calculations have been performed with the computational resources provided by the bwUniCluster project [77]. We acknowledge financial support from the EU project QTFLAG, the BMBF via Q.com, and the Eliteprogramm for Postdocs of the Baden–Württemberg Stiftung via the TESLA.G project. S.M. gratefully acknowledges the support of the DFG via a Heisenberg fellowship and the TWITTER project.

Appendix A: Numerical methods

As mentioned above, we employ TN methods as our simulation tool. The ground state properties have been obtained via imaginary time evolution for MPS [44], or via variational minimization for TTN [53, 78]. In order to obtain thermal equilibrium states for $T > 0$, we use imaginary time evolution applied to LPTN. Each discretization step of this evolution generates a fixed-temperature state, starting from the maximally mixed state (infinite temperature). The temperature of the LPTN after n steps is inversely proportional to n , i.e. $T \propto 1/n$. In the following, we summarize the LPTN framework in more detail, beginning with a brief recap of MPS notation.

The idea of MPS is the decomposition of a many-body wave function $|\psi\rangle$ representing a system on L sites into a set of L local tensors which compose together $|\psi\rangle$. The original vector representing the quantum many-body state has d^L entries, where d is the local dimension of the Bose–Hubbard model in our case. Each tensor represents one site and is of rank-3, $T_{\alpha_j, i_j, \alpha_{j+1}}$; the index i_j iterates over the different states in the local Hilbert space, i.e. the Fock states on site j , and the indices α connect the

site to their nearest neighbor and encode the entanglement to the complete subsystem on the left and right, respectively. The maximal dimension of α enables us to truncate entanglement and to keep simulations feasible; this maximal dimension is called bond dimension m . For $m = d^{L/2}$ the MPS representation covers all possible states, i.e. the full Hilbert space.

The idea of the LPTN lies in the positivity of a density matrix, i.e., we can decompose any density matrix ρ as

$$\rho = U\Lambda U^\dagger = U\sqrt{\Lambda}\sqrt{\Lambda}U^\dagger = XX^\dagger, \quad (\text{A1})$$

where $\Lambda_i \geq 0$ are the eigenvalues represented in a diagonal matrix Λ , and we define $X \equiv U\sqrt{\Lambda}$. The matrix X is the purification of the density matrix ρ and is sufficient for the unitary time evolution and imaginary time evolution, as outlined later on. The purification X scales with the system size as $d^L \times 1$ for a pure state and $d^L \times d^L$ for a maximally mixed state $\rho \propto \mathbb{1}$. For the special case of a pure state, there is exactly one eigenvalue equal to one and $\rho = |\psi\rangle\langle\psi|$. We can include this new index running over the eigenvalues by extending each tensor in the MPS with an additional index κ_j , i.e., $T_{\alpha_j, i_j, \kappa_j, \alpha_{j+1}}$; we obtain the LPTN. The MPS is regained for $\dim(\kappa_j) = 1, \forall j$. In contrast, if each $\dim(\kappa_j) = d, \forall j$, we regain, globally, the dimension d^L of the matrix Λ .

We turn to the argument why this representation is efficient in the case of finite-temperature states. We define the thermal state as $\rho_{\text{th}} = \exp(-\beta H)/Z$ with the partition function defined as $Z = \text{Tr}[\exp(-\beta H)]$. We can rewrite the thermal state as

$$\begin{aligned} \rho_{\text{th}} &= \frac{\exp(-\beta H)}{Z} \\ &= \frac{1}{Z} \exp\left(-\frac{\beta H}{2}\right) \mathbb{1} \exp\left(-\frac{\beta H}{2}\right), \end{aligned} \quad (\text{A2})$$

where the identity $\mathbb{1}$ is proportional to the infinite-temperature state ρ_{inf} ; its purification can be easily represented as an LPTN, where the global identity is a product state of local identities with $\dim(\alpha_j) = 1, \forall j$; the identity matrix is with respect to the indices i_j and κ_j for each site j . Equation (A2) represents the imaginary time evolution with a constant Hamiltonian. For the real-time evolution, we time-slice the Hamiltonian and evolve the state under a Hamiltonian constant for each time step Δt . To approximate the propagator of the Hamiltonian in both time evolution schemes, we use a Suzuki-Trotter decomposition splitting the Hamiltonian into $H = H_{2j-1,2j} + H_{2j,2j+1}$, where $H_{2j-1,2j}$ acts on odd sites and their nearest right neighbor, and the second term contains operators acting on even sites and the nearest right neighbor. There is an error scaling with Δt when using

$$\begin{aligned} \exp(cH) &= \exp\left(\frac{c}{2}H_{2j-1,2j}\right) \exp(cH_{2j,2j+1}) \\ &\quad \times \exp\left(\frac{c}{2}H_{2j-1,2j}\right) + \mathcal{O}(\Delta t^3), \end{aligned} \quad (\text{A3})$$

where the summands in each exponential on the right-hand side commute with each other and, consequently,

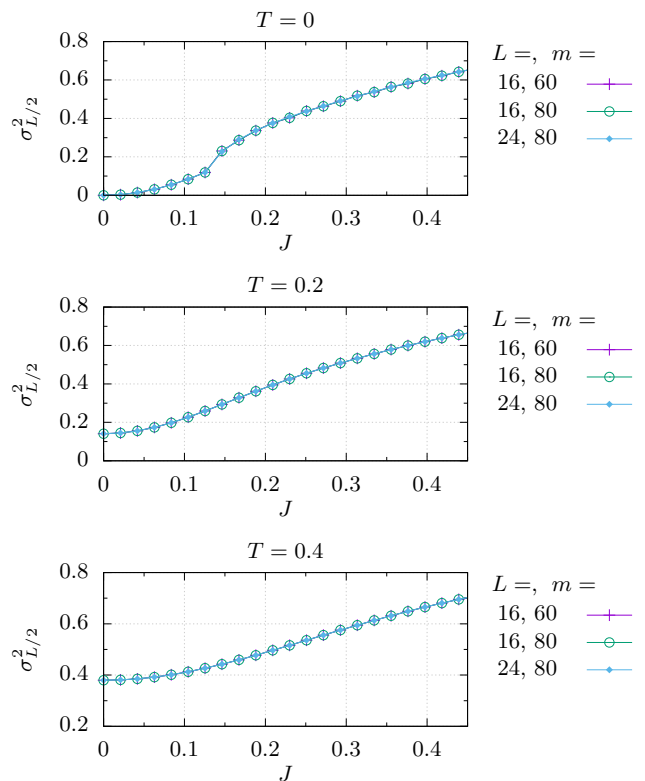


FIG. 9. (Color online) Demonstration of convergence in the system size L and the bond dimension m for the variance in the middle of the chain as a function of the hopping strength J . Local dimension $d = 5$, and $U = 1, \mu = 1/2$.

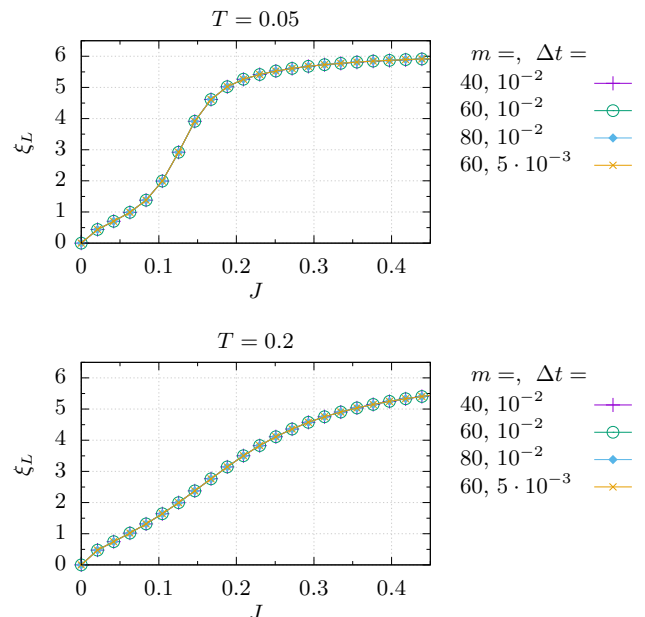


FIG. 10. (Color online) Demonstration of convergence in the bond dimension m and the Trotter time step Δt for the correlation length ξ_L as a function of the hopping strength J . The system size is $L = 16$, the local dimension is $d = 5$, and $U = 1, \mu = 1/2$.

can be exponentiated independently on the local two-site Hilbert spaces. The constant c is $i\Delta t$ and Δt for the real and the imaginary time evolution, respectively. The error of the total evolution scales as $\mathcal{O}(\Delta t^2)$ for this second order Suzuki-Trotter decomposition. The application of each of the three layers follows the idea of the TEBD algorithm [44, 62]. We point out that it is sufficient to evolve either X or X^\dagger because both real and imaginary time evolution preserve the complex conjugate structure of the purification.

In addition to errors scaling with the time step Δt , we have to truncate correlations in the dimension of α_j . For an exact representation of a many-body state, the number of weights at the center of our many-body representation can include up to d^L non-zero weights in the case of an LPTN, or $d^{L/2}$ for a pure state represented as an MPS. We allow for truncations of small weights in the spectrum of the singular value decomposition (SVD). The truncation with the SVD results in a minimal error for the evolution of an LPTN [49] if the LPTN is properly gauged [46]. The index κ_j capturing the purification is not growing during a unitary time evolution and guarantees an efficient evolution.

Appendix B: Convergence of the simulations

In this section we show with some examples that the numerical simulations presented above are at convergence with respect to changing the relevant refinement parameters. In our case, these include the system size L , the bond dimension m , the Trotter time step Δt and the local dimension d .

In Fig. 9 we demonstrate that the variances of the particle occupations of the obtained equilibrium ground- and thermal states are independent of the system size L . The deviations of $\sigma_{L/2}^2(J)$ are below point size when changing both the system size L and the bond dimension m , for all considered values of the temperature T .

The two plots in Fig. 10 show that the Trotter time step Δt and the employed bond dimensions m are sufficient for converged imaginary time evolution results: The error of the correlation length ξ_L is again below point size.

Figure 11 illustrates how we numerically obtain the compressibilities plotted in Fig. 1: We first determine the filling ρ as a function of the chemical potential μ , and then linearly fit this data in an interval of width $\Delta\mu$ around $\mu = 1/2$, yielding an estimate for the compressibility $\partial\rho/\partial\mu|_{\mu=1/2}$. We plot $\rho(\mu)$ for two different values of J in the upper two panels of Fig. 11, demonstrating that $\partial\rho/\partial\mu$ indeed only vanishes in the Mott insulator phase. For a system at zero temperature and finite size L , the filling $\rho = N/L$ is limited to integer multiples of $1/L$, leading to a step-like behavior of $\rho(\mu)$. In order to account for this finite-size effect, a careful choice of the fit interval $\Delta\mu$ is required. We find that $\Delta\mu = 0.15$ provides a good trade-off in the parameter regime studied here, see lower panel of Fig. 11.

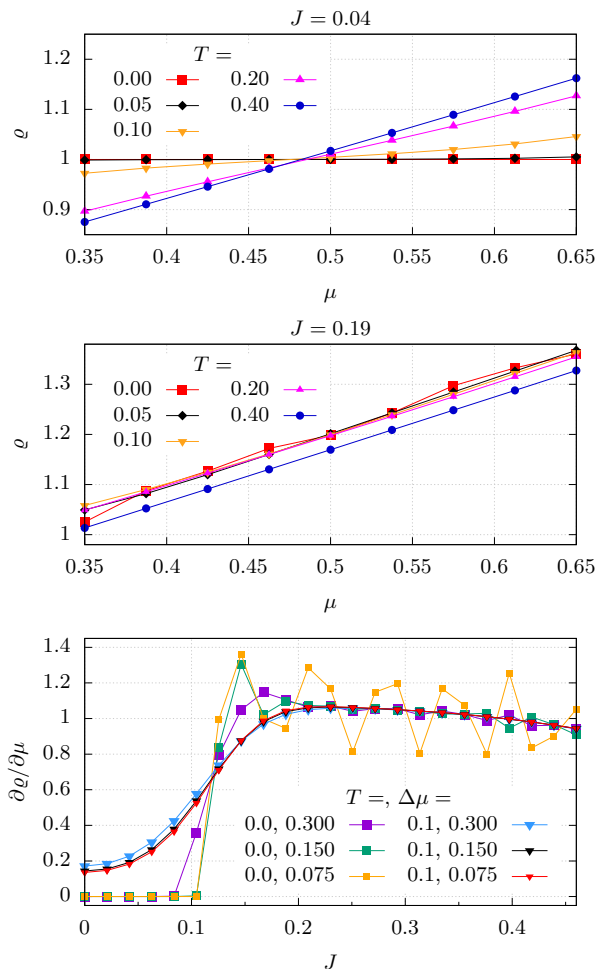


FIG. 11. (Color online) Numerical calculation of the compressibility $\partial\rho/\partial\mu$: The upper two panels show the filling ρ as a function of the chemical potential μ , for various temperatures and two hopping strengths $J = 0.04 < J_c$ and $J = 0.19 > J_c$. The lower panel shows the fitted slopes $\Delta\rho/\Delta\mu$ as a function of the hopping strength J , for two different temperatures and three different values for the fit interval $\Delta\mu$. The system size is $L = 18$, and $U = 1$.

Finally, in Fig. 12 we focus on the convergence of the quench data presented in Sec. III. It is evident that both for zero (upper panel) and finite temperature (lower panel) the local dimension $d = 4$ delivers noticeably different results compared to $d = 5$. Instead, the observed deviations between $d = 5$ and $d \geq 6$ become negligibly small.

Appendix C: Analytical treatment of time evolution for short quenches

Here we show the calculation leading to Eq. (11). We start from the perfect Mott insulator state with fill-

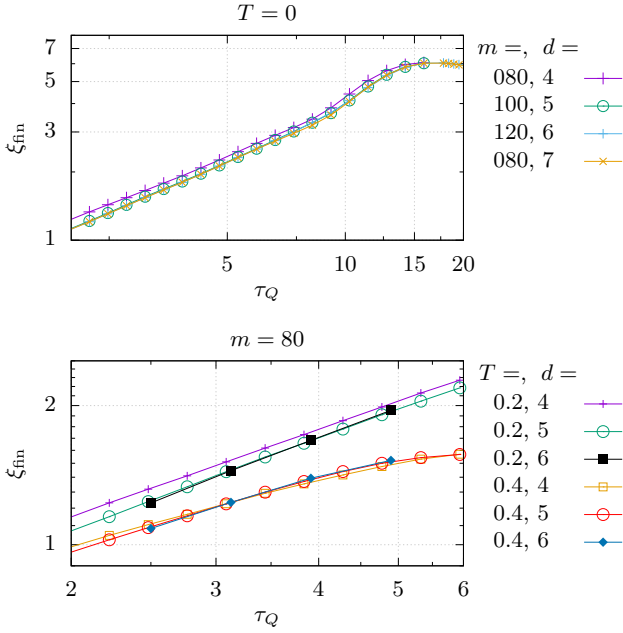


FIG. 12. (Color online) Demonstration of convergence in the bond dimension m and local dimension d for the final correlation length ξ_{fin} as a function of the quench time τ_Q . The upper panel corresponds to the results presented in Fig. 7, the lower panel to the ones in Fig. 8. The system size is $L = 16$.

ing $\varrho = 1$, i.e.

$$|\Psi_0\rangle = |\Psi(-\tau_Q/2)\rangle = |1\rangle_1 \dots |1\rangle_L. \quad (\text{C1})$$

Performing a linear quench in the hopping strength entails a non-trivial time evolution under the time-dependent Hamiltonian $H(t)$. We focus on the case $\tau_Q \ll 1$, meaning the total evolution time is short. Discretizing the integration of the Schrödinger equation we can write

$$|\Psi(\tau_Q/2)\rangle \simeq \left(1 - i\bar{H}\tau_Q - \frac{1}{2}\bar{H}^2\tau_Q^2 + \mathcal{O}(\tau_Q^3)\right) |\Psi_0\rangle, \quad (\text{C2})$$

and we use the trapezoidal rule to determine the constant Hamiltonian \bar{H} during the discretization interval $[-\tau_Q/2, \tau_Q/2]$:

$$\bar{H} = \frac{1}{2} [H(-\tau_Q/2) + H(\tau_Q/2)] = H(J(0)) = H(J_c), \quad (\text{C3})$$

where we used the definition of the linear ramp $J(t)$ of Eq. (8).

Plugging Eqs. (C1) and (C3) into Eq. (C2), we can calculate the final state $|\Psi(\tau_Q/2)\rangle$, exact up to third order in τ_Q (here we assume periodic boundary conditions for simplicity, and $U = 1$):

$$\begin{aligned} |\Psi(\tau_Q/2)\rangle &= (1 - 2\tau_Q^2 J_c^2 L) |1\rangle_1 \dots |1\rangle_L \\ &+ \left(\frac{1}{\sqrt{2}} \tau_Q^2 J_c + i\sqrt{2} \tau_Q J_c\right) \sum_{j=1}^L |1\rangle_1 \dots |1\rangle_{j-1} \left(|2\rangle_j |0\rangle_{j+1} + |0\rangle_j |2\rangle_{j+1}\right) |1\rangle_{j+2} \dots |1\rangle_L \\ &- 2\tau_Q^2 J_c^2 \sum_{j=1}^L \sum_{k>j+1}^L |1\rangle_1 \dots |1\rangle_{j-1} \left(|2\rangle_j |0\rangle_{j+1} + |0\rangle_j |2\rangle_{j+1}\right) |1\rangle_{j+2} \dots |1\rangle_{k-1} \left(|2\rangle_k |0\rangle_{k+1} + |0\rangle_k |2\rangle_{k+1}\right) |1\rangle_{k+2} \dots |1\rangle_L \\ &- \frac{3}{\sqrt{2}} \tau_Q^2 J_c^2 \sum_{j=1}^L |1\rangle_1 \dots |1\rangle_{j-1} \left(|2\rangle_j |1\rangle_{j+1} |0\rangle_{j+2} + |0\rangle_j |1\rangle_{j+1} |2\rangle_{j+2}\right) |1\rangle_{j+3} \dots |1\rangle_L \\ &- \sqrt{6} \tau_Q^2 J_c^2 \sum_{j=1}^L |1\rangle_1 \dots |1\rangle_{j-1} |0\rangle_j |3\rangle_{j+1} |0\rangle_{j+2} |1\rangle_{j+3} \dots |1\rangle_L \\ &+ \mathcal{O}(\tau_Q^3). \end{aligned} \quad (\text{C4})$$

From Eq. (C4) we obtain the two-site hopping correlations, again exact up to third order in τ_Q :

$$\langle b_j^\dagger b_k \rangle = \begin{cases} 1, & \text{for } j = k \\ 2\tau_Q^2 J_c + \mathcal{O}(\tau_Q^3), & \text{for } |j - k| = 1 \\ \mathcal{O}(\tau_Q^3), & \text{for } |j - k| > 1 \end{cases} \quad (\text{C5})$$

We can use these to determine the correlation length ξ_{fin} according to Eq. (4):

$$\begin{aligned} \xi_{\text{fin}} &= \sqrt{\frac{2L \cdot 1^2 \cdot 2\tau_Q^2 J_c + \mathcal{O}(\tau_Q^3)}{L + 2L \cdot 2\tau_Q^2 J_c + \mathcal{O}(\tau_Q^3)}} \\ &= 2\sqrt{J_c} \tau_Q + \mathcal{O}(\tau_Q^2), \end{aligned} \quad (\text{C6})$$

which is the expression used in Eq. (11).

-
- [1] D. Jaksch, C. Bruder, J. I. Cirac, C. W. Gardiner, and P. Zoller, *Phys. Rev. Lett.* **81**, 3108 (1998).
- [2] D. Jaksch and P. Zoller, *Annals of Physics* **315**, 52 (2005).
- [3] M. Lewenstein, A. Sanpera, V. Ahufinger, B. Damski, A. Sen(De), and U. Sen, *Advances in Physics* **56**, 243 (2007).
- [4] W. S. Bakr, A. Peng, M. E. Tai, R. Ma, J. Simon, J. I. Gillen, S. Fölling, L. Pollet, and M. Greiner, *Science* **329**, 547 (2010).
- [5] I. Bloch, J. Dalibard, and W. Zwerger, *Rev. Mod. Phys.* **80**, 885 (2008).
- [6] I. Bloch and A. Rosch, *Phys. Status Solidi B* **247**, 530 (2010).
- [7] C. Gross and I. Bloch, *Science* **357**, 995 (2017).
- [8] M. Greiner, O. Mandel, T. Esslinger, T. W. Hänsch, and I. Bloch, *Nature* **415**, 39 (2002).
- [9] B. Paredes, A. Widera, V. Murg, O. Mandel, S. Fölling, I. Cirac, G. V. Shlyapnikov, T. W. Hänsch, and I. Bloch, *Nature* **429**, 277 (2004).
- [10] T. Stöferle, H. Moritz, C. Schori, M. Köhl, and T. Esslinger, *Phys. Rev. Lett.* **92**, 130403 (2004).
- [11] I. Spielman, W. Phillips, and J. Porto, *Phys. Rev. Lett.* **98**, 080404 (2007).
- [12] H. A. Gersch and G. C. Knollman, *Phys. Rev.* **129**, 959 (1963).
- [13] M. P. A. Fisher, P. B. Weichman, G. Grinstein, and D. S. Fisher, *Phys. Rev. B* **40**, 546 (1989).
- [14] T. D. Kühner, S. R. White, and H. Monien, *Phys. Rev. B* **61**, 12474 (2000).
- [15] K. V. Krutitsky, *Phys. Rep.* **607**, 1 (2016).
- [16] D. C. McKay and B. DeMarco, *Rep. Prog. Phys.* **74**, 054401 (2011).
- [17] F. Gerbier, *Phys. Rev. Lett.* **99**, 120405 (2007).
- [18] W.-J. Hu and N.-H. Tong, *Phys. Rev. B* **80**, 245110 (2009).
- [19] D. Dalidovich and M. P. Kennett, *Phys. Rev. A* **79**, 053611 (2009).
- [20] A. Hoffmann and A. Pelster, *Phys. Rev. A* **79**, 053623 (2009).
- [21] A. S. Hassan, *Physica B: Condensed Matter* **405**, 3766 (2010).
- [22] K. W. Mahmud, E. N. Duchon, Y. Kato, N. Kawashima, R. T. Scalettar, and N. Trivedi, *Phys. Rev. B* **84**, 054302 (2011).
- [23] I. Spielman, W. Phillips, and J. Porto, *Phys. Rev. Lett.* **100**, 120402 (2008).
- [24] D. McKay, M. White, and B. DeMarco, *Phys. Rev. A* **79**, 063605 (2009).
- [25] K. Jiménez-García, R. L. Compton, Y.-J. Lin, W. D. Phillips, J. V. Porto, and I. B. Spielman, *Phys. Rev. Lett.* **105**, 110401 (2010).
- [26] S. Trotzky, L. Pollet, F. Gerbier, U. Schnorrberger, I. Bloch, N. V. Prokof'ev, B. Svistunov, and M. Troyer, *Nat. Phys.* **6**, 998 (2010).
- [27] L. Gori, T. Barthel, A. Kumar, E. Lucioni, L. Tanzi, M. Inguscio, G. Modugno, T. Giamarchi, C. D'Errico, and G. Roux, *Phys. Rev. A* **93**, 033650 (2016).
- [28] C. Kollath, U. Schollwöck, J. von Delft, and W. Zwerger, *Phys. Rev. A* **71**, 053606 (2005).
- [29] O. Morsch and M. Oberthaler, *Rev. Mod. Phys.* **78**, 179 (2006).
- [30] C. Kollath, A. M. Läuchli, and E. Altman, *Phys. Rev. Lett.* **98**, 180601 (2007).
- [31] S. Trotzky, Y.-A. Chen, A. Flesch, I. P. McCulloch, U. Schollwöck, J. Eisert, and I. Bloch, *Nat. Phys.* **8**, 325 (2012).
- [32] A. Daley, H. Pichler, J. Schachenmayer, and P. Zoller, *Phys. Rev. Lett.* **109**, 020505 (2012).
- [33] J.-S. Bernier, R. Tan, L. Bonnes, C. Guo, D. Poletti, and C. Kollath, *Phys. Rev. Lett.* **120**, 020401 (2018).
- [34] T. W. Kibble, *J. Phys. A: Math. Gen.* **9**, 1387 (1976).
- [35] W. H. Zurek, *Nature* **317**, 505 (1985).
- [36] W. H. Zurek, U. Dorner, and P. Zoller, *Phys. Rev. Lett.* **95**, 105701 (2005).
- [37] J. Dziarmaga and M. M. Rams, *New J. Phys.* **12**, 055007 (2010).
- [38] J. Dziarmaga and W. H. Zurek, *Scientific Reports* **4**, 5950 (2014).
- [39] S. Braun, M. Friesdorf, S. S. Hodgman, M. Schreiber, J. P. Ronzheimer, A. Riera, M. del Rey, I. Bloch, J. Eisert, and U. Schneider, *Proc. Natl. Acad. Sci. U.S.A.* **112**, 3641 (2015).
- [40] K. Shimizu, Y. Kuno, T. Hirano, and I. Ichinose, *Phys. Rev. A* **97**, 033626 (2018).
- [41] A. Dutta, A. Rahmani, and A. del Campo, *Phys. Rev. Lett.* **117**, 080402 (2016).
- [42] S. Yin, C.-Y. Lo, and P. Chen, *Phys. Rev. B* **94**, 064302 (2016).
- [43] Z.-P. Gao, D.-W. Zhang, Y. Yu, and S.-L. Zhu, *Phys. Rev. B* **95**, 224303 (2017).
- [44] U. Schollwöck, *Annals of Physics* **326**, 96 (2011).
- [45] R. Orús, *Annals of Physics* **349**, 117 (2014).
- [46] P. Silvi, F. Tschirsich, M. Gerster, J. Jünemann, D. Jaschke, M. Rizzi, and S. Montangero, *ArXiv e-prints* **1710.03733** (2017).
- [47] F. Verstraete, J. J. García-Ripoll, and J. I. Cirac, *Phys. Rev. Lett.* **93**, 207204 (2004).
- [48] G. de las Cuevas, N. Schuch, D. Pérez-García, and J. I. Cirac, *New J. Phys.* **15**, 123021 (2013).
- [49] A. Werner, D. Jaschke, P. Silvi, M. Kliesch, T. Calarco, J. Eisert, and S. Montangero, *Phys. Rev. Lett.* **116**, 237201 (2016).
- [50] D. Jaschke, S. Montangero, and L. D. Carr, *Quantum Science and Technology* (2018), 10.1088/2058-9565/aae724.
- [51] D. Pérez García, F. Verstraete, M. M. Wolf, and J. I. Cirac, *Quantum Information & Computation* **7**, 401 (2007).
- [52] Y.-Y. Shi, L.-M. Duan, and G. Vidal, *Phys. Rev. A* **74**, 022320 (2006).
- [53] M. Gerster, P. Silvi, M. Rizzi, R. Fazio, T. Calarco, and S. Montangero, *Phys. Rev. B* **90**, 125154 (2014).
- [54] T. D. Kühner and H. Monien, *Phys. Rev. B* **58**, R14741 (1998).
- [55] N. D. Mermin and H. Wagner, *Phys. Rev. Lett.* **17**, 1133 (1966).
- [56] P. C. Hohenberg, *Phys. Rev.* **158**, 383 (1967).
- [57] T. Giamarchi, *Physica B: Condensed Matter* **230-232**, 975 (1997).
- [58] Note that this is different from the scenario studied in Sec. II, where not the filling ρ but the chemical potential μ was kept constant.

- [59] V. L. Berezinskii, *Sov. Phys. JETP* **34**, 610 (1972).
- [60] J. M. Kosterlitz and D. J. Thouless, *J. Phys. C: Solid State Phys.* **6**, 1181 (1973).
- [61] N. Laflorencie, *Phys. Rep.* **646**, 1 (2016).
- [62] G. Vidal, *Phys. Rev. Lett.* **93**, 040502 (2004).
- [63] B. Gardas, J. Dziarmaga, and W. H. Zurek, *Phys. Rev. B* **95**, 104306 (2017).
- [64] J. M. Kosterlitz, *J. Phys. C: Solid State Phys.* **7**, 1046 (1974).
- [65] S. Arrhenius, *Zeitschrift für physikalische Chemie* **4**, 96 (1889).
- [66] B. Capogrosso-Sansone, N. V. Prokof'ev, and B. V. Svistunov, *Phys. Rev. B* **75**, 134302 (2007).
- [67] G. G. Batrouni, V. Rousseau, R. T. Scalettar, M. Rigol, A. Muramatsu, P. J. H. Denteneer, and M. Troyer, *Phys. Rev. Lett.* **89**, 117203 (2002).
- [68] S. van Frank, M. Bonneau, J. Schmiedmayer, S. Hild, C. Gross, M. Cheneau, I. Bloch, T. Pichler, A. Negretti, T. Calarco, and S. Montangero, *Scientific Reports* **6**, 34187 (2016).
- [69] S. Yin, P. Mai, and F. Zhong, *Phys. Rev. B* **89**, 094108 (2014).
- [70] S. Yin, C.-Y. Lo, and P. Chen, *Phys. Rev. B* **93**, 184301 (2016).
- [71] A. Kossakowski, *Rep. Math. Phys.* **3**, 247 (1972).
- [72] G. Lindblad, *Commun. Math. Phys.* **48**, 119 (1976).
- [73] V. Gorini, A. Kossakowski, and E. C. G. Sudarshan, *J. Math. Phys.* **17**, 821 (1976).
- [74] H.-P. Breuer and F. Petruccione, *The Theory of Open Quantum Systems*, 1st ed. (Clarendon Press, Oxford, 2009).
- [75] I. de Vega and D. Alonso, *Rev. Mod. Phys.* **89**, 015001 (2017).
- [76] E. Mascarenhas and I. de Vega, *Phys. Rev. A* **96**, 062117 (2017).
- [77] bwUniCluster: funded by the Ministry of Science, Research and Arts and the universities of the state of Baden-Württemberg, Germany, within the framework program bwHPC.
- [78] L. Tagliacozzo, G. Evenbly, and G. Vidal, *Phys. Rev. B* **80**, 235127 (2009).